

Electronic structure and superconducting properties of LaNiO_2

Ziyan Chen,^{1,2} Yuxin Wang,^{1,2} Kun Jiang,^{1,2,*} and Jiangping Hu^{1,3,4,†}

¹Beijing National Laboratory for Condensed Matter Physics and Institute of Physics, Chinese Academy of Sciences, Beijing 100190, China

²School of Physical Sciences, University of Chinese Academy of Sciences, Beijing 100190, China

³Kavli Institute of Theoretical Sciences, University of Chinese Academy of Sciences, Beijing, 100190, China

⁴New Cornerstone Science Laboratory, Beijing, 100190, China

(Dated: November 7, 2024)

Motivated by recent photoemission measurements on the $\text{La}_{0.8}\text{Sr}_{0.2}\text{NiO}_2$, we carry out a systematic study of the infinite-layer nickelate using both dynamical mean-field theory and density matrix embedding theory. The renormalized electronic structure and Fermi surface of correlated $\text{La}_{0.8}\text{Sr}_{0.2}\text{NiO}_2$ are studied in an effective two-band model through the dynamical mean-field calculation. We find the correlation effects reflect mainly on the Ni d band, which is consistent with the experimental findings. We further study the ground state including magnetism and superconductivity through the density matrix embedding theory. Within the experimental doping range and rigid-band approximation, we show that the d -wave superconductivity is the lowest energy state, while the static magnetism is absent except very close to zero doping. These findings provide a new understanding of infinite-layer nickelate superconductivity.

The pairing mechanism of high-temperature (high T_c) superconductors (SCs) is one of the most important questions in condensed matter [1–3]. Since the discovery of cuprates [1], tremendous efforts have been spent on finding new high-temperature superconductors. As a neighborhood of copper, nickelates have long been proposed as an ideal system for realizing high T_c SC [4, 5]. This proposal becomes true after the infinite-layer nickelate $\text{Nd}_{0.8}\text{Sr}_{0.2}\text{NiO}_2$ ($T_c \sim 15$ K) thin films are synthesized using the soft-chemistry topotactic reduction method [6, 7]. This infinite-layer LnNiO_2 ($\text{Ln}=\text{La, Nd, Pr}$) opens a new window for nickelate SCs [8–14]. Recently, the family of nickelate SCs have been extended to $\text{La}_3\text{Ni}_2\text{O}_7$, $\text{La}_4\text{Ni}_3\text{O}_{10}$ under pressure [15–21].

On the other hand, determining LnNiO_2 electronic structure is crucial to understanding its superconductivity. Owing to their special structures and the CaH_2 reduction method [6], it has been difficult to directly probe the electronic structure through angle-resolved photoemission spectroscopy (ARPES), scanning tunneling microscopy (STM) and other related techniques. Only very recently, the $\text{La}_{0.8}\text{Sr}_{0.2}\text{NiO}_2$ electronic structures were successfully measured by ARPES for the first time using the molecular beam epitaxy (MBE) and in situ atomic-hydrogen reduction methods [22, 23]. These findings call for new theoretical calculations to determine correct minimal models for the nickelate superconductors. In this work, we carry out a systematic study of LnNiO_2 using both modern dynamical mean-field theory (DMFT) and density matrix embedding theory (DMET). We find that the renormalized electronic structure and Fermi surface of correlated $\text{La}_{0.8}\text{Sr}_{0.2}\text{NiO}_2$ measured in the experiments can be quantitatively obtained in an effective two-band minimal model through the dynamical mean-field calculation. Furthermore, we also predict that the d -wave superconductivity is the lowest energy state and there is no static magnetism except close to zero doping for the nickelate superconductors.

Just like the cuprates SCs, the central component of LnNiO_2 is the NiO_2 plane, where Ni forms a square lattice and O sites at the bond connecting each Ni atom as

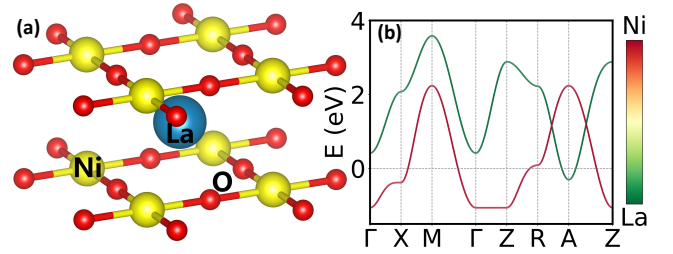


FIG. 1. (a) Schematic plot of the LaNiO_2 crystal structure, where the blue, yellow, and red atoms represent La, Ni, and O elements, respectively; The central ingredient for LaNiO_2 electronic structure is the NiO_2 plane. (b) The band structure of the low-energy two-orbital effective model for $\text{La}_{0.8}\text{Sr}_{0.2}\text{NiO}_2$. The orbital content of Ni $3d_{x^2-y^2}$ and La $5d$ are projected to the color bar between red (Ni) and green (La).

shown in Fig.1(a). The Ln atoms are sandwiched between two NiO_2 planes. Since the ARPES experiments focus on the $\text{La}_{0.8}\text{Sr}_{0.2}\text{NiO}_2$, we apply the density functional theory (DFT) to this hole-doped LnNiO_2 . Our DFT calculations employ the Vienna ab-initio simulation package (VASP) code [24] with the projector augmented wave (PAW) method [25]. The Perdew-Burke-Ernzerhof (PBE) [26] exchange-correlation functional is used in our calculation. The cutoff energy for expanding the wave functions into a plane-wave basis is set to be 500 eV. The energy convergence criterion is 10^{-8} eV. The Γ -centered $13 \times 13 \times 15$ k-meshes are used. The lattice relaxation parameters obtained from VASP calculations were $a = b = 3.93$ Å, and $c = 3.38$ Å. Then, based on the two-orbital model for infinite-layer nickelates proposed in previous studies [27], we construct the low-energy effective two-band Hamiltonian to describe the electronic structure at hole doping $x = 0.2$. The tight-binding (TB) model in the basis $(c_{1k\sigma}, c_{2k\sigma})$ as

$$H_t(\mathbf{k}) = \begin{pmatrix} \epsilon_{11}(\mathbf{k}) & \epsilon_{12}^*(\mathbf{k}) \\ \epsilon_{12}(\mathbf{k}) & \epsilon_{22}(\mathbf{k}) \end{pmatrix}, \quad (1)$$

where 1, 2 is the orbital index for Ni and La respectively and $\epsilon_{\alpha\beta}(\mathbf{k})$ is the hopping function defined in the supplemental materials (SMs). The corresponding non-interacting electronic structure is plotted in Fig.1(b). We want to add a note here. The DFT calculated Fermi surface (FSs) is slightly different than the ARPES measurements [22, 23]. This is most likely owing to the changes in electronic structure caused by the correlation effect. We take the approximation that the correlation effect for La electrons is weak as in Ref. [12], which is absorbed into the TB parameters. Hence, we slightly change the TB parameters to match the experimental FSs. It turns out this is an efficient and effective choice. The comparison between TB and DFT is listed in SMs.

From the TB results in Fig.1(b), we can find that the Ni $3d_{x^2-y^2}$ orbital (red color) contributes the most valence electrons around the Fermi level (E_F), which is similar to hole-doped cuprates with electron occupation between $3d^9$ to $3d^8$. On the other hand, most of La $5d$ contributions are above E_F with a small Fermi pocket around A point. This topological structure of FSs is consistent with experimental observation at this doping [22]. Notice that previous theoretical reports also show that there is another electron Fermi pocket around the Γ point at this doping, which is absent in our results and experiments [22, 23]. Additionally, owing to the z -direction coupling, the Ni $3d_{x^2-y^2}$ electronic band is not strictly quasi-2-dimensional resulting in the van-hove point below E_F (X point) at $k_z = 0$ plane and above E_F (R point) at $k_z = \pi$ plane.

After obtaining the TB model, we treat the electronic correlations beyond DFT to study band renormalization. Following previous strategy [12] and experimental observations, we only add the Hubbard interaction to Ni 3d-electrons as

$$H_{int} = U \sum_i \hat{n}_{i1\uparrow} \hat{n}_{i1\downarrow} \quad (2)$$

and neglect the correlation effects of 5d-electrons as discussed above. Then, we employ the DMFT method to the $H_t + H_{int}$ and calculate the spectral function of $\text{La}_{0.8}\text{Sr}_{0.2}\text{NiO}_2$. The DMFT calculations are performed using the open-source TRIQS package [28, 29] with the continuous-time Monte Carlo impurity solver based on the strong-coupling expansion [30]. The temperature is set to 290 K and U is set to 3.1 eV for the calculations as in Ref. [12]. The self-energy $\Sigma(\omega)$ is obtained by the analytical continuation from imaginary frequency to real frequency using the maximum entropy method [31].

We first look at the FSs and DMFT obtained spectral function $A(k, \omega = 0)$ results as plotted in Fig.2 (a) and (b). In the $k_z = 0$ plane in Fig.2 (a), there is one FS centering around the Brillouin zone (BZ) corner, which shows a similar contour as hole-doped cuprates. The calculated FS matches well with the ARPES observed FS (yellow triangles) in Fig.2 (a) [22]. Then, moving to the $k_z = \pi$ plane, there are two groups of FSs. At the BZ corner, a small electron pocket from 5-d electron shows up as discussed above. At the BZ center, the 3d hole FS in $k_z = 0$ plane evolves into the electron FS in $k_z = \pi$ plane. The feature indicates the Ni 3d-electron has

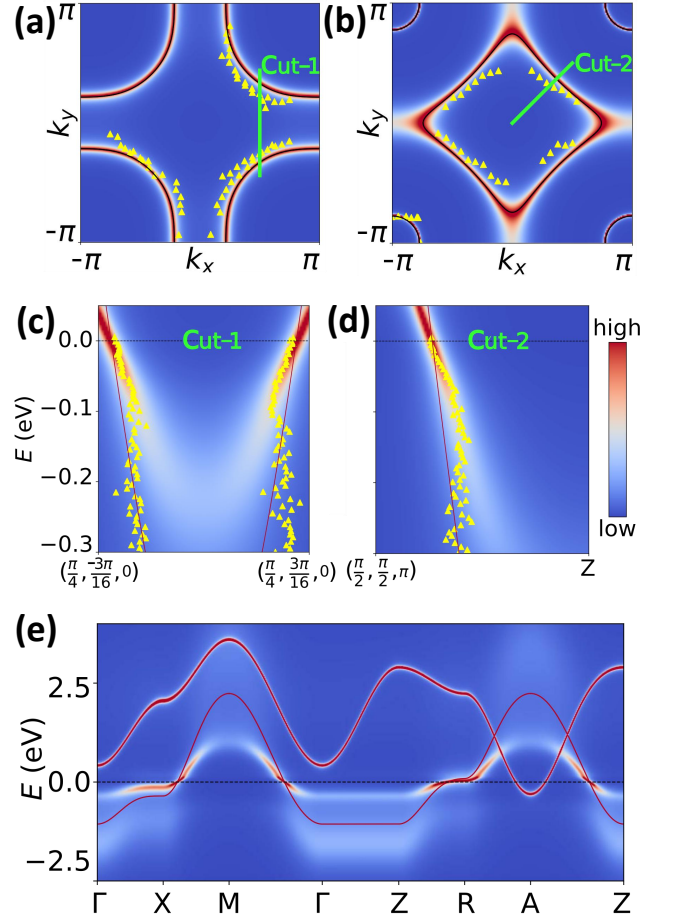


FIG. 2. (a-b) The Fermi surfaces and spectral function $A(k, \omega = 0)$ plots at $k_z=0$ and $k_z=\pi$, respectively. (c), (d) The spectral function slices of $\text{La}_{0.8}\text{Sr}_{0.2}\text{NiO}_2$ obtained using the DMFT method along different k -paths. The spectral function slices of $\text{La}_{0.8}\text{Sr}_{0.2}\text{NiO}_2$ obtained using the DMFT method along Cut-1 and Cut-2 at (a-b). The yellow triangles represent the experimental data [22], and the red solid line represents the TB results. (e) The renormalized $A(k, \omega)$ and non-interacting TB bands along the high-symmetry lines.

a strong k_z dependence, as discussed above. We also notice that the $A(k, \omega = 0)$ in Fig. 2 (a) remains sharp around the non-interacting Fermi points while the $A(k, \omega = 0)$ in Fig. 2 (b) becomes much broader owing to the van-hove points. This distinct feature may influence the electronic properties of LnNiO_2 .

Besides the FSs, the band renormalization effect can be captured well by the DMFT calculation. The renormalized spectral function $A(k, \omega)$ along the high-symmetry point is plotted in Fig.2 (e). We can see the 5d band remains unrenormalized owing to the uncorrelated approximation. As listed in SM, the 5d band mass from TB, DFT and experiments are almost the same without considering their bands' position shifting. This feature is consistent with the 5d band is highly over-doped from its half-filling resulting in a weakly renormalized band. On the other hand, the 3d quasiparticle $A(k, \omega)$ around E_F in-

dicates a renormalized band. In Fig. 2(c-d), the renormalized $A(k, \omega)$ and ARPES data are compared. We find $A(k, \omega)$ agrees well with experimental data around the Fermi level. In ARPES data, additional dispersion anomaly emerges below -0.1 eV, which is most likely a correlation effect beyond our current approach [22]. By comparing the Fermi velocity v_F without renormalization and v_F at $A(k, \omega)$, we find the renormalization factor is about 0.3 at $k_z = 0$ plane and 0.36 at $k_z = \pi$ plane.

We further explore the ground state of LaNiO_2 . We apply the DMET method developed in recent years [32]. The DMET is an efficient cluster embedding method for dealing with strongly correlated systems[32]. Its basic principle is very similar to the DMFT method, where a lattice system is mapped onto a finite-size impurity problem. The density matrix between the bulk and impurity is matched after achieving self-consistency. DMET has been applied the three-band model of cuprates [33, 34]. In the following calculations, we use the two-band model of $\text{La}_{0.8}\text{Sr}_{0.2}\text{NiO}_2$ discussed above. The Hubbard interaction $U = 3.1$ eV is applied to 3d-electrons while treating 5d-electrons as non-interacting.

In our calculation, a 2×2 supercell with 4 Ni and 4 La atoms is selected as the impurity cluster, as illustrated in Fig.3 (a). The total lattice size is chosen to be $40 \times 40 \times 20$ unit cells. The most relevant symmetry-breaking phases for the single-band Hubbard model are the antiferromagnetic (AFM) ordering at (π, π) and d -wave superconductivity. Hence, we introduce the pairing terms and magnetic terms in the correlation potential. The calculations focus on the experimental-related hole-doped region, up to a doping level x of 0.4. Furthermore, since the DMFT calculated FS of the La band is the same as the TB model, we fix the electron density of La as in the TB model at each self-consistent DMET calculation. The rigid band shift of the TB model is used for the doping change.

The DMET impurity solver used in our calculations is the open-source Block2 package [35]. Block2 package implements the density matrix renormalization group (DMRG) as the impurity solver. The maximum bond dimension is chosen to be 800. The tolerance for the DMRG sweep energy was set to 10^{-6} . To extract the magnetic and superconducting properties of the system, we define the antiferromagnetic order parameter $m = \frac{1}{4} \sum_i |m_i|$, where m_i is the local magnetic moment on the Ni or La atoms, and the summation is taken over the four Ni atoms in the 2×2 supercell. Similarly, the superconducting order parameter is defined as $\Delta_{SC} = \sum_{\langle i'j' \rangle} \frac{1}{\sqrt{2}} [\langle d_{i\alpha} d_{j\beta} \rangle + \langle d_{j\alpha} d_{i\beta} \rangle]$ where the summation is taken over pairs of neighboring Ni or La atoms in the 2×2 supercell. The notation $\langle \dots \rangle$ refers to the reduced single-particle density matrix elements in the Nambu basis.

The self-consistent DMET calculations depend on the initial ansatz for the correlation potential, which determines the bulk symmetry-breaking effects. For the pairing part, we introduce d -wave superconducting pairing on the nearest-neighbor Ni orbitals, while pairing in other channels was not prohibited in the subsequent self-consistent calculations. For the magnetism part, we consider both paramagnetic and anti-

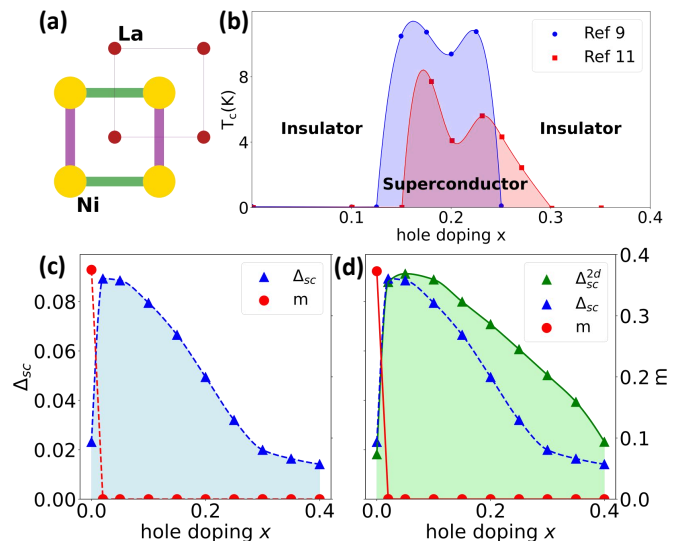


FIG. 3. (a) The impurity cluster of LaNiO_2 for the DMET calculation. We use yellow and red to represent Ni and La atoms, respectively. The area of the circles represents the charge occupation on each atom, and the width and color of the lines between atoms represent the superconducting pairing strength and its sign. (b) The experimental phase diagrams of LnNiO_2 measured in $\text{Nd}_{1-x}\text{Sr}_x\text{NiO}_2$ [9] and $\text{La}_{1-x}\text{Ca}_x\text{NiO}_2$ [11]. (c) The magnitude of the superconducting Δ_{SC} and magnetic order m parameters at different levels of hole doping. The magnetic axis is at the right axis (red). The calculations were performed using a 2×2 DMET cluster based on the TB model in Eq.1, with the interaction on the Ni $d_{x^2-y^2}$ orbital set to $U = 3.1$ eV. (d) The phase diagram determined by DMET based on the TB model without z-direction hopping. The superconducting order parameter is labeled by Δ_{SC}^{2d} while the dash blue line represents the phase boundary in (c).

ferromagnetic initial guesses. The convergence criteria are set to be less than 10^{-5} for the ground state energy and magnetic moments, and 10^{-4} for the superconducting order parameter. Typically, the calculations converge within 20 iterations.

The results of self-consistent DMET calculation based on the TB and Hubbard interaction are summarized in Fig.3(c). Interestingly, no magnetism has been found in the hole-doping region from the DMET calculation except for x very close to 0. There are two possible reasons for this feature. The Ni 3d-band is away from the half-filling in this region. At $x = 0$, the filling fraction of 3d-electron is about $n_{Ni} = 0.978$. It is known that the AFM of cuprates vanishes around $n_{Cu} = 0.98 \sim 0.95$ [3] and the antiferromagnetic (AF) super-exchange coupling of Ni is weaker than Cu [36]. Furthermore, the itinerant La 5d-electron can further reduce the magnetism. Hence, the magnetic boundary is around $x = 0$.

Considering the superconducting order parameter Δ_{SC} , a d -wave ground state is always obtained in this doping region. We also try the s -wave ansatz, which always evolves into the d -wave channel during iteration. From the phase diagram in Fig.3(c), the largest Δ_{SC} is obtained around $x = 0.05$ which keeps decreasing with hole doping. The feature is consis-

tent with previous cuprates calculations, where the electron-electron pairing is from AF spin exchange. The AF fluctuation becomes much stronger when close to its half-filling. The La 5d-electrons without correlation also acquire weak superconductivity owing to the coupling between Ni and La.

As discussed in the Fig. 2, the $\text{La}_{0.8}\text{Sr}_{0.2}\text{NiO}_2$ hosts a strong 3-dimension electronic structure. This 3-dimensional feature may influence its superconducting order parameters. It is experimentally proposed that hydrogen can effectively tune the dimensionality of nickelates FSs [37] inducing superconducting dome feature. To capture this effect, we modify the hopping parameters in the TB model by ignoring the z-direction hopping. The resulting FSs become purely two-dimensional except for weak deviation owing to La electrons. Then, we apply the same approach as above. The obtained phase diagram is shown in Fig. 3 (d). The magnetism is still missing although we have tried the AFM ansatz as the initial input. It is interesting that the dimensionality indeed influences the Δ_{SC}^{2d} order parameters, especially at the large doping region. This enhancement becomes much weaker when approaching $x = 0$. Hence, reducing the dimensionality of nickelates can indeed enhance the superconductivity.

Although DMET comprehensively studies the infinite layer nickelates, the phase diagram still deviates from the experiment findings [9, 11]. Let's look at the up-to-date phase diagram of LnNiO_2 from various experimental groups [9, 11], as plotted in Fig. 3 (b). There is a superconducting dome ranging from $x = 0.1$ to $x = 0.3$. Beyond this dome, two insulating regions emerge. LnNiO_2 is always a dirty and disordered system due to their reduction methods. Compared with cuprates, the disorder may play a more important role in LnNiO_2 physical properties.

For the $x > 0.3$ region, this region is already on the tail of our DMET SC region. It is well-known that the nodal d -wave superconductivity is more sensitive to disorder. Hence, no superconductivity identified in this region is reasonable due to reduction and doping-induced disorder.

On the contrary, the insulating $x < 0.1$ region is completely different. In principle, the largest pairing order parameters in this region from our DMET calculation and previous understandings should be more robust than $0.1 < x < 0.3$ region. Recently, a superconducting state has been reported near $x = 0$ parent NdNiO_2 [38, 39]. Therefore, we believe this region will still be superconducting if the sample is pure without disorder. The insulating behavior in this region is highly nontrivial owing to the interplay of disorder and strong correlation [40], which calls for further exploration. Improving the sample quality and other controllable reduction methods is needed.

In conclusion, we conduct a comprehensive study of infinite-layer nickelates using dynamical mean-field theory and density matrix embedding theory. Starting with density functional calculations and experimental data, we construct an effective two-band tight-binding model. We then use DMFT to examine the renormalized electronic structure and Fermi surface of the correlated compound $\text{La}_{0.8}\text{Sr}_{0.2}\text{NiO}_2$. We find

that the correlation effects primarily impact the Ni 3d-band, in agreement with experimental observations. Leveraging this reliable model, we study the ground state properties of nickelates including magnetism and superconductivity via DMET. Within the doping range and under the rigid-band approximation, we identify d -wave superconductivity as the ground state and there is no static magnetism except close to $x = 0$. The relation between our calculation and the experimental phase diagram is further discussed. Our findings contribute to a new understanding of superconductivity in infinite-layer nickelates.

When finalizing this manuscript, we notice a similar DMFT study of nickelates [41], which arrives at a similar conclusion.

Acknowledgement We thank Dr. Zhi-Hao Cui and Bo Zhan for the useful discussion and help in DMET. We acknowledge the support by the Ministry of Science and Technology (Grant No. 2022YFA1403900), the National Natural Science Foundation of China (Grant No. NSFC-11888101, No. NSFC-12174428, No. NSFC-11920101005), the Strategic Priority Research Program of the Chinese Academy of Sciences (Grant No. XDB28000000, XDB33000000), the New Cornerstone Investigator Program, and the Chinese Academy of Sciences Project for Young Scientists in Basic Research (2022YSBR-048).

* jiangkun@iphy.ac.cn

† jphu@iphy.ac.cn

- [1] J. G. Bednorz and K. A. Müller, "Possible high t_c superconductivity in the ba-la-cu-o system," *Zeitschrift für Physik B Condensed Matter* **64**, 189–193 (1986).
- [2] Patrick A. Lee, Naoto Nagaosa, and Xiao-Gang Wen, "Doping a mott insulator: Physics of high-temperature superconductivity," *Rev. Mod. Phys.* **78**, 17–85 (2006).
- [3] B. Keimer, S. A. Kivelson, M. R. Norman, S. Uchida, and J. Zaanen, "From quantum matter to high-temperature superconductivity in copper oxides," *Nature* **518**, 179–186 (2015).
- [4] V. I. Anisimov, D. Bukhvalov, and T. M. Rice, "Electronic structure of possible nickelate analogs to the cuprates," *Phys. Rev. B* **59**, 7901–7906 (1999).
- [5] K.-W. Lee and W. E. Pickett, "Infinite-layer LaNiO_2 : n_i^{1+} is not cu^{2+} ," *Phys. Rev. B* **70**, 165109 (2004).
- [6] Danfeng Li, Kyuho Lee, Bai Yang Wang, Motoki Osada, Samuel Crossley, Hye Ryoung Lee, Yi Cui, Yasuyuki Hikita, and Harold Y. Hwang, "Superconductivity in an infinite-layer nickelate," *Nature* **572**, 624–627 (2019).
- [7] Michael R. Norman, "Entering the Nickel Age of Superconductivity," *Physics* **13**, 85 (2020).
- [8] Motoki Osada, Bai Yang Wang, Kyuho Lee, Danfeng Li, and Harold Y. Hwang, "Phase diagram of infinite layer praseodymium nickelate $\text{pr}_{1-x}\text{sr}_x\text{nio}_2$ thin films," *Phys. Rev. Mater.* **4**, 121801 (2020).
- [9] Danfeng Li, Bai Yang Wang, Kyuho Lee, Shannon P. Harvey, Motoki Osada, Berit H. Goodge, Lena F. Kourkoutis, and Harold Y. Hwang, "Superconducting dome in $\text{nd}_{1-x}\text{sr}_x\text{nio}_2$ infinite layer films," *Phys. Rev. Lett.* **125**, 027001 (2020).
- [10] Kyuho Lee, Bai Yang Wang, Motoki Osada, Berit H. Goodge, Tiffany C. Wang, Yonghun Lee, Shannon Harvey, Woo Jin Kim, Yijun Yu, Chaitanya Murthy, Srinivas Raghu, Lena F. Kourk-

- outis, and Harold Y. Hwang, “Linear-in-temperature resistivity for optimally superconducting (nd,sr)nio₂,” *Nature* **619**, 288–292 (2023).
- [11] Shengwei Zeng, Changjian Li, Lin Er Chow, Yu Cao, Zhaoting Zhang, Chi Sin Tang, Xinmao Yin, Zhi Shiuh Lim, Junxiong Hu, Ping Yang, and Ariando Ariando, “Superconductivity in infinite-layer nickelate La_{1-x}Ca_xNiO₂ thin films,” *Science Advances* **8**, eabl9927 (2022).
- [12] Jonathan Karp, Antia S. Botana, Michael R. Norman, Hyowon Park, Manuel Zingl, and Andrew Millis, “Many-body electronic structure of ndnio₂ and cacuo₂,” *Phys. Rev. X* **10**, 021061 (2020).
- [13] Frank Lechermann, “Multiorbital processes rule the nd_{1-x}sr_xnio₂ normal state,” *Phys. Rev. X* **10**, 041002 (2020).
- [14] Francesco Petocchi, Viktor Christiansson, Fredrik Nilsson, Ferdi Aryasetiawan, and Philipp Werner, “Normal state of nd_{1-x}sr_xnio₂ from self-consistent gw + EDMFT,” *Phys. Rev. X* **10**, 041047 (2020).
- [15] Hualei Sun, Mengwu Huo, Xunwu Hu, Jingyuan Li, Zengjia Liu, Yifeng Han, Lingyun Tang, Zhongquan Mao, Pengtao Yang, Bosen Wang, Jinguang Cheng, Dao-Xin Yao, Guang-Ming Zhang, and Meng Wang, “Signatures of superconductivity near 80 k in a nickelate under high pressure,” *Nature* **621**, 493–498 (2023).
- [16] Yanan Zhang, Dajun Su, Yanen Huang, Zhaoyang Shan, Hualei Sun, Mengwu Huo, Kaixin Ye, Jiawen Zhang, Zihan Yang, Yongkang Xu, Yi Su, Rui Li, Michael Smidman, Meng Wang, Lin Jiao, and Huiqiu Yuan, “High-temperature superconductivity with zero resistance and strange-metal behaviour in La₃Ni₂O_{7-δ},” *Nature Physics* **20**, 1269–1273 (2024).
- [17] Jun Hou, Peng-Tao Yang, Zi-Yi Liu, Jing-Yuan Li, Peng-Fei Shan, Liang Ma, Gang Wang, Ning-Ning Wang, Hai-Zhong Guo, Jian-Ping Sun, Yoshiya Uwatoko, Meng Wang, Guang-Ming Zhang, Bo-Sen Wang, and Jin-Guang Cheng, “Emergence of High-Temperature Superconducting Phase in Pressurized La₃Ni₂O₇ Crystals,” *Chinese Physics Letters* **40**, 117302 (2023).
- [18] Hirofumi Sakakibara, Masayuki Ochi, Hibiki Nagata, Yuta Ueki, Hiroya Sakurai, Ryo Matsumoto, Kensei Terashima, Keisuke Hirose, Hiroto Ohta, Masaki Kato, Yoshihiko Takano, and Kazuhiko Kuroki, “Theoretical analysis on the possibility of superconductivity in the trilayer ruddlesden-popper nickelate la₄ni₃o₁₀ under pressure and its experimental examination: Comparison with la₃ni₂o₇,” *Phys. Rev. B* **109**, 144511 (2024).
- [19] Yinghao Zhu, Di Peng, Enkang Zhang, Bingying Pan, Xu Chen, Lixing Chen, Huifen Ren, Feiyang Liu, Yiqing Hao, Nana Li, Zhenfang Xing, Fujun Lan, Jiyuan Han, Junjie Wang, Donghan Jia, Hongliang Wo, Yiqing Gu, Yimeng Gu, Li Ji, Wenbin Wang, Huiyang Gou, Yao Shen, Tianping Ying, Xiaolong Chen, Wenge Yang, Huibo Cao, Changlin Zheng, Qiaoshi Zeng, Jiangang Guo, and Jun Zhao, “Superconductivity in pressurized trilayer La₄Ni₃O_{10-δ} single crystals,” *Nature* **631**, 531–536 (2024).
- [20] Qing Li, Ying-Jie Zhang, Zhe-Ning Xiang, Yuhang Zhang, Xiyu Zhu, and Hai-Hu Wen, “Signature of superconductivity in pressurized la₄ni₃o₁₀,” *Chinese Physics Letters* **41**, 017401 (2024).
- [21] Mingxin Zhang, Cuiying Pei, Xian Du, Weixiong Hu, Yantao Cao, Qi Wang, Juefei Wu, Yidian Li, Huanyu Liu, Chenhaoping Wen, Yi Zhao, Changhua Li, Weizheng Cao, Shihao Zhu, Qing Zhang, Na Yu, Peihong Cheng, Lili Zhang, Zhiwei Li, Jinkui Zhao, Yulin Chen, Hanjie Guo, Congjun Wu, Fan Yang, Shichao Yan, Lexian Yang, and Yanpeng Qi, “Superconductivity in trilayer nickelate la₄ni₃o₁₀ under pressure,” (2024), arXiv:2311.07423 [cond-mat.supr-con].
- [22] Wenjie Sun, Zhicheng Jiang, Chengliang Xia, Bo Hao, Yueying Li, Shengjun Yan, Maosen Wang, Hongquan Liu, Jianyang Ding, Jiayu Liu, Zhengtai Liu, Jishan Liu, Hanghui Chen, Dawei Shen, and Yuefeng Nie, “Electronic structure of superconducting infinite-layer lanthanum nickelates,” (2024), arXiv:2403.07344 [cond-mat.supr-con].
- [23] Xiang Ding, Yu Fan, Xiaoxiao Wang, Chihao Li, Zhitong An, Jiahao Ye, Shenglin Tang, Minyinan Lei, Xingtian Sun, Nan Guo, Zhihui Chen, Suppanut Sangphet, Yilin Wang, Haichao Xu, Rui Peng, and Donglai Feng, “Cuprate-like electronic structures in infinite-layer nickelates with substantial hole dopings,” *National Science Review* **11**, nwae194 (2024).
- [24] G. Kresse and J. Furthmüller, “Efficient iterative schemes for ab initio total-energy calculations using a plane-wave basis set,” *Phys. Rev. B* **54**, 11169–11186 (1996).
- [25] G. Kresse and D. Joubert, “From ultrasoft pseudopotentials to the projector augmented-wave method,” *Phys. Rev. B* **59**, 1758–1775 (1999).
- [26] John P Perdew, Kieron Burke, and Matthias Ernzerhof, “Generalized gradient approximation made simple,” *Physical review letters* **77**, 3865 (1996).
- [27] Jiacheng Gao, Shiyu Peng, Zhijun Wang, Chen Fang, and Hongming Weng, “Electronic structures and topological properties in nickelates Lnn+1NinO2n+2,” *National Science Review* **8**, nwaa218 (2020).
- [28] Olivier Parcollet, Michel Ferrero, Thomas Ayrat, Hartmut Hafermann, Igor Krivenko, Laura Messio, and Priyanka Seth, “Triqs: A toolbox for research on interacting quantum systems,” *Computer Physics Communications* **196**, 398–415 (2015).
- [29] Maximilian Merkel, Alberto Carta, Sophie Beck, and Alexander Hampel, “solid-dmft: gray-boxing DFT+DMFT materials simulations with TRIQS,” *Journal of Open Source Software* **7**, 4623 (2022).
- [30] Priyanka Seth, Igor Krivenko, Michel Ferrero, and Olivier Parcollet, “Triqs/cthyb: A continuous-time quantum monte carlo hybridisation expansion solver for quantum impurity problems,” *Computer Physics Communications* **200**, 274–284 (2016).
- [31] Gernot J. Kraberger, Robert Triebl, Manuel Zingl, and Markus Aichhorn, “Maximum entropy formalism for the analytic continuation of matrix-valued green’s functions,” *Phys. Rev. B* **96**, 155128 (2017).
- [32] Gerald Knizia and Garnet Kin-Lic Chan, “Density matrix embedding: A simple alternative to dynamical mean-field theory,” *Phys. Rev. Lett.* **109**, 186404 (2012).
- [33] Zhi-Hao Cui, Chong Sun, Ushnish Ray, Bo-Xiao Zheng, Qiming Sun, and Garnet Kin-Lic Chan, “Ground-state phase diagram of the three-band hubbard model from density matrix embedding theory,” *Phys. Rev. Res.* **2**, 043259 (2020).
- [34] Zhi-Hao Cui, Tianyu Zhu, and Garnet Kin-Lic Chan, “Efficient implementation of ab initio quantum embedding in periodic systems: Density matrix embedding theory,” *Journal of Chemical Theory and Computation* **16**, 119–129 (2020).
- [35] Huanchen Zhai, Henrik R. Larsson, Seunghoon Lee, Zhi-Hao Cui, Tianyu Zhu, Chong Sun, Linqing Peng, Ruoqing Peng, Ke Liao, Johannes Tölle, Junjie Yang, Shuoxue Li, and Garnet Kin-Lic Chan, “Block2: A comprehensive open source framework to develop and apply state-of-the-art DMRG algorithms in electronic structure and beyond,” *The Journal of Chemical Physics* **159**, 234801 (2023).
- [36] Mi Jiang, Mona Berciu, and George A. Sawatzky, “Critical nature of the ni spin state in doped ndnio₂,” *Phys. Rev. Lett.* **124**, 207004 (2020).

- [37] Xiang Ding, Charles C. Tam, Xuelei Sui, Yan Zhao, Minghui Xu, Jaewon Choi, Huaqian Leng, Ji Zhang, Mei Wu, Haiyan Xiao, Xiaotao Zu, Mirian Garcia-Fernandez, Stefano Agrestini, Xiaoqiang Wu, Qingyuan Wang, Peng Gao, Sean Li, Bing Huang, Ke-Jin Zhou, and Liang Qiao, “Critical role of hydrogen for superconductivity in nickelates,” *Nature* **615**, 50–55 (2023).
- [38] C. T. Parzyck, Y. Wu, L. Bhatt, M. Kang, Z. Arthur, T. M. Pedersen, R. Sutarto, S. Fan, J. Pellicciari, V. Bisogni, G. Heranz, A. B. Georgescu, D. G. Hawthorn, L. F. Kourkoutis, D. A. Muller, D. G. Schlom, and K. M. Shen, “Superconductivity in the parent infinite-layer nickelate NdNiO_2 ,” (2024), [arXiv:2410.02007 \[cond-mat.supr-con\]](https://arxiv.org/abs/2410.02007).
- [39] Danfeng Li, “Infinite-layer nickelate superconductor,” (2025), Talk at Beijing Forum on high temperature superconductivity 2025.
- [40] Y.-T. Hsu, M. Osada, B. Y. Wang, M. Berben, C. Duffy, S. P. Harvey, K. Lee, D. Li, S. Wiedmann, H. Y. Hwang, and N. E. Hussey, “Correlated insulating behavior in infinite-layer nickelates,” *Frontiers in Physics* **10** (2022), [10.3389/fphy.2022.846639](https://doi.org/10.3389/fphy.2022.846639).
- [41] Liang Si, Eric Jacob, Wenfeng Wu, Andreas Hausoel, Juraj Kršnik, Paul Worm, Simone Di Cataldo, Oleg Janson, and Karsten Held, “Closing in on possible scenarios for infinite-layer nickelates: comparison of dynamical mean-field theory with angular-resolved photoemission spectroscopy,” (2024), [arXiv:2408.12985 \[cond-mat.supr-con\]](https://arxiv.org/abs/2408.12985).

Supplemental Material

TABLE S1. The hopping parameters for the two-band model Hamiltonians(with z-direction hopping).All the units are eV.

$t_{11}^{(0,0,0)}$	0.4024	$t_{22}^{(0,0,0)}$	1.8872
$t_{11}^{(1,0,0)}$	-0.4125	$t_{22}^{(1,0,0)}$	0.0013
$t_{11}^{(0,0,1)}$	-0.0538	$t_{22}^{(0,0,1)}$	0.0650
$t_{11}^{(1,1,0)}$	0.0894	$t_{22}^{(1,1,0)}$	-0.0606
$t_{11}^{(1,0,1)}$	0.000	$t_{22}^{(1,0,1)}$	-0.1980
$t_{11}^{(1,1,1)}$	0.0134	$t_{22}^{(1,1,1)}$	0.0281
$t_{11}^{(2,0,0)}$	-0.0430	$t_{22}^{(2,0,0)}$	0.000
$t_{12}^{(1,0,0)}$	0.0196		

APPENDIX A: BAND STRUCTURE

The two bands Hamiltonian for LnNiO_2 can be written in the following form:

$$H(k) = \begin{pmatrix} H_{11} & H_{12} \\ H_{21} & H_{22} \end{pmatrix} \quad (\text{S1})$$

where subscripts 1 and 2 correspond to the Ni and La atoms, respectively. The specific form of the diagonal terms is given by:

$$\begin{aligned} H_{\alpha\alpha} = & t_{\alpha\alpha}^{(0,0,0)} + 2t_{\alpha\alpha}^{(1,0,0)} (\cos k_x + \cos k_y) \\ & + 2t_{\alpha\alpha}^{(0,0,1)} \cos k_z + 4t_{\alpha\alpha}^{(1,1,0)} \cos k_x \cos k_y \\ & + 4t_{\alpha\alpha}^{(1,0,1)} \cos k_z (\cos k_x + \cos k_y) \\ & + 8t_{\alpha\alpha}^{(1,1,1)} \cos k_x \cos k_y \cos k_z \\ & + 2t_{\alpha\alpha}^{(1,0,0)} (\cos 2k_x + \cos 2k_y) \end{aligned} \quad (\text{S2})$$

The values of the hopping matrix elements are listed in Table.S1. Here, H_{12} denotes the hopping between the La and Ni atoms. Due to symmetry considerations, the nearest-neighbor hopping matrix element vanishes, and the next-nearest-neighbor hopping takes the following form:

$$H_{12} = t_{12}^{(1,0,0)} (1 + e^{ik_z}) (2 \cos k_x - 2 \cos k_y) \quad (\text{S3})$$

Naturally, we have $H_{21} = H_{12}^*$.

In our calculations, we also investigated the effect of the system's two-dimensionality on its superconducting properties. Specifically, we restricted the hopping of electrons in the Ni $d_{x^2-y^2}$ orbitals to within the X-Y plane by manually setting the hopping matrix elements in the Z direction to zero. The Hamiltonian retains the same form as previously given, with parameters as listed in Table S2.

In Fig.S1, the blue lines represent the band structure results obtained from Density Functional Theory (DFT) calculations, while the black dashed lines correspond to the band structure derived from the Hamiltonian using the parameters listed in Table S1.

TABLE S2. The hopping parameters for the two-band model Hamiltonians(without z-direction hopping).All the units are eV.

$t_{11}^{(0,0,0)}$	0.4024	$t_{22}^{(0,0,0)}$	1.8872
$t_{11}^{(1,0,0)}$	-0.4125	$t_{22}^{(1,0,0)}$	0.0013
$t_{11}^{(0,0,1)}$	0.000	$t_{22}^{(0,0,1)}$	0.0650
$t_{11}^{(1,1,0)}$	0.0894	$t_{22}^{(1,1,0)}$	-0.0606
$t_{11}^{(1,0,1)}$	0.000	$t_{22}^{(1,0,1)}$	-0.1980
$t_{11}^{(1,1,1)}$	0.000	$t_{22}^{(1,1,1)}$	0.0281
$t_{11}^{(2,0,0)}$	-0.0430	$t_{22}^{(2,0,0)}$	0.000
$t_{12}^{(1,0,0)}$	0.0196		

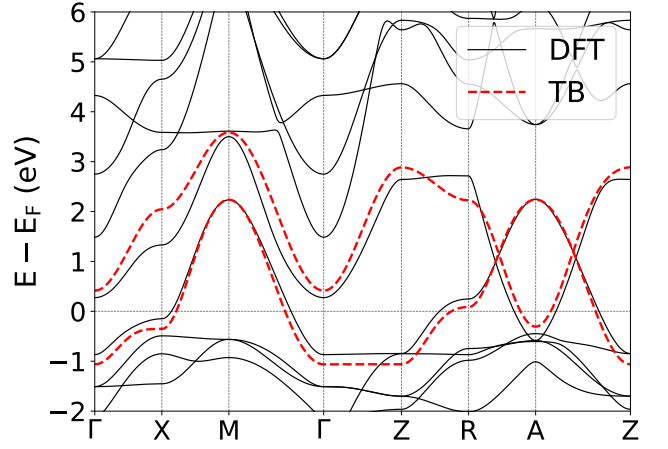


FIG. S1. A comparison between Density Functional Theory (DFT) and the two-band model along high-symmetry points in the reciprocal space. The black solid lines represent the DFT results, while the red dashed lines correspond to the two-band model used in our work.

APPENDIX B: DMFT RESULT

In Fig.S2, we provide more comparison between the spectral function results in the $k_z = 0$ plane and the experimental data. Compared to the non-interacting DFT bands, interactions lead to a band renormalization of approximately 2.62. Panel (b) of Fig.S2 focuses on the electron-like pocket of 5d electrons near the $A(\pi, \pi, \pi)$ point in the Brillouin zone. We also plot the 5d-band (black line in Fig.S2(b)) from DFT. Although we shift the position of 5d band, the effective mass of 5d band remains almost unchanged between DFT and TB. Since the correlation effect is weak for 5d electrons in our approximation, the DMFT calculation does not significantly alter the band structure, and the size and depth of the pocket match well with the experimental data. Hence, we can safely say the correlation in 5d is irrelevant to our problem.

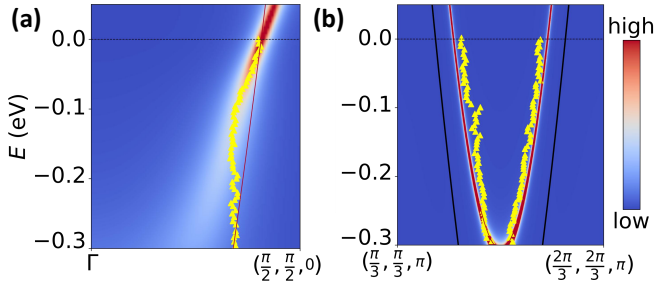


FIG. S2. Comparison of the DMFT spectral function with experimental data along specific paths. The red solid lines represent the bands obtained from two-band model Hamiltonian, while the yellow triangles denote the experimental data. (a) Spectral function along the path from $\Gamma (0,0,0)$ to $(\pi/2, \pi/2, 0)$. (b) Spectral function along the path from $(\pi/3, \pi/3, \pi)$ to $(2\pi/3, 2\pi/3, \pi)$, the solid black line indicates the DFT result.

APPENDIX C: DMET RESULT

The final phase diagrams, both with and without z-direction hopping, are presented in the main text. However, to obtain these phase diagrams, it is crucial to carefully calculate the energy and superconducting pairing symmetry for different initial magnetic states. Fig. S4 shows order parameter values in different two-band model and different initial magnetic states. For the paramagnetic initial state, whether the model includes z-direction hopping or not, the magnetism is suppressed to very small values. In contrast, for the antiferromagnetic initial guess, the antiferromagnetic order parameter decreases as doping increases, and when the doping reaches around 0.25, even with an antiferromagnetic initial guess, the magnetism converges to a very small value or even to zero.

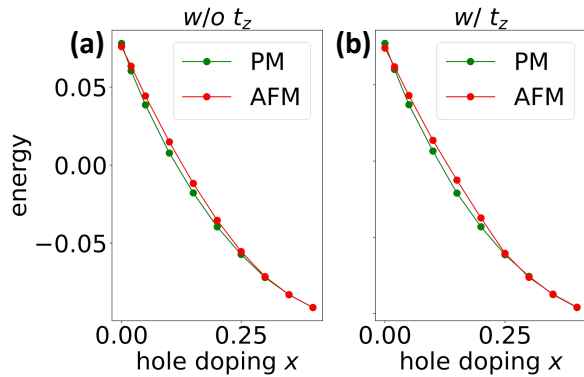


FIG. S3. The ground state energies of two-band models under different doping levels, where the green and red lines represent the paramagnetic and antiferromagnetic initial guesses, respectively. (a) Ground state energies obtained by converging from paramagnetic and antiferromagnetic initial guesses under the model parameters without z-direction hopping. (b) Ground state energies obtained by converging from paramagnetic and antiferromagnetic initial guesses under the model parameters with z-direction hopping.

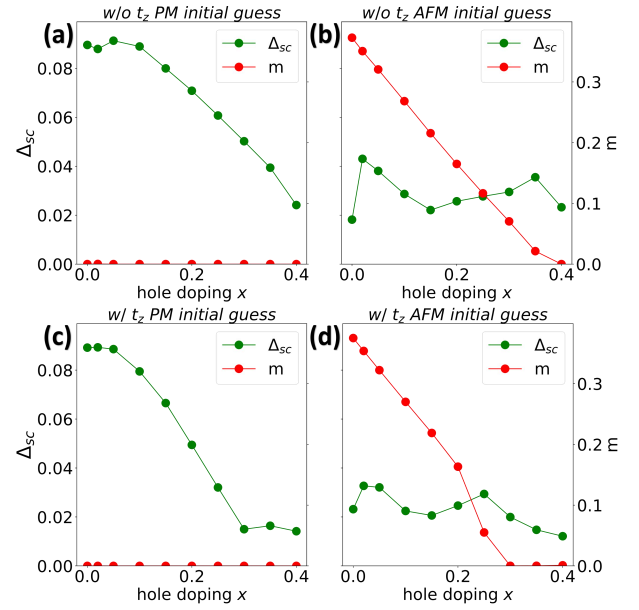


FIG. S4. The superconducting and magnetic order parameters as a function of doping, obtained from different initial magnetic states: (a) The model without z-direction hopping and paramagnetic initial state. (b) The model without z-direction hopping and antiferromagnetic initial state. (c) The model with z-direction hopping and paramagnetic initial state. (d) The model with z-direction hopping and antiferromagnetic initial state.

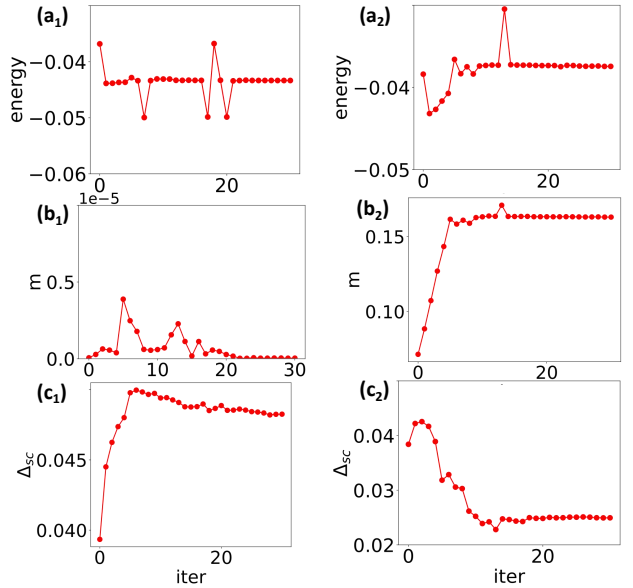


FIG. S5. The evolution of energy, magnetism, and superconductivity during the self-consistent iterations. The left column corresponds to the model with z-direction hopping at hole doping $x = 0.2$, using the paramagnetic state as the initial guess for the self-consistent iteration, while the right column uses the antiferromagnetic state as the initial guess. (a1), (a2) Energy as a function of the iteration steps. (b1), (b2) Magnetism as a function of the iteration steps. (c1), (c2) Superconducting order parameter as a function of the iteration steps.

To determine which state corresponds to the true physical state, we need to consider the energy for different initial magnetic states. Fig.S3 shows the energies after convergence for different initial conditions. It can be observed that when doping is greater than 0.25, the ground state energies for both initial guesses are nearly identical, as can also be seen from the phase diagram in Fig.S4. When doping is between 0.02 and 0.25, the paramagnetic ground state energy is always lower than the antiferromagnetic one. It is worth noting that within a very small doping range near half-filling (approximately 0.01), the ground state energy of the antiferromagnetic state

becomes lower. This indicates that the system is antiferromagnetic near half-filling, and with the addition of a small amount of doping, the system quickly transitions to a paramagnetic state.

Fig.S5 illustrates the convergence behavior of energy, magnetism, and superconductivity during the DMET calculations. In our computations, the ground state energy and magnetism generally stabilize rapidly after a few iterations. However, the convergence of the superconducting order parameter is slower, with varying speeds depending on the doping range, but it is generally slower than that of energy and magnetism.